Dreiling, J., Tilmann, F., Yuan, X., Giese, J., Rindraharisaona, E. J., Rümpker, G., Wysession, M. E. (2018): Crustal Radial Anisotropy and Linkage to Geodynamic Processes: A Study Based on Seismic Ambient Noise in Southern Madagascar. - *Journal of Geophysical Research*, *123*, 6, pp. 5130—5146.

DOI: http://doi.org/10.1029/2017JB015273

Journal of Geophysical Research: Solid Earth

RESEARCH ARTICLE
10.1029/2017JB015273

Crustal Radial Anisotropy and Linkage to Geodynamic Processes: A Study Based on Seismic Ambient Noise in Southern Madagascar

Jennifer Dreiling[1,2], Frederik Tilmann[1,2], Xiaohui Yuan[1], Jörg Giese[2], Elisa J. Rindraharisaona[1,3], Georg Rümpker[4], and Michael E. Wysession[5]

[1]GFZ German Research Centre for Geosciences, Potsdam, Germany, [2]Freie Universität Berlin, Berlin, Germany, [3]Institute and Observatory of Geophysics, University of Antananarivo, Antananarivo, Madagascar, [4]Institute of Geosciences, Goethe-Universität Frankfurt, Frankfurt am Main, Germany, [5]Department of Earth and Planetary Sciences, Washington University, Saint Louis, USA

Abstract We determined radial anisotropy in the crust of southern Madagascar from the differences between the speeds of vertically and horizontally polarized shear waves (V_{SV} and V_{SH}), which we derived from Rayleigh and Love wave dispersion determined from seismic ambient noise correlations. The amalgamated Precambrian units in the east and the Phanerozoic Morondava basin in the west of southern Madagascar were shaped by different geodynamic processes. The crystalline basement was strongly deformed and metamorphosed to varying degrees during the assembly of Gondwana in the Pan-African Orogeny, whereas the Morondava basin was completed with the separation of Africa and Madagascar. The different developments are reflected in first-order differences in the radial anisotropy patterns. In the Precambrian domains, positive anisotropy ($V_{SV} < V_{SH}$) is found in the upper and lower crust, with a layer of negative anisotropy ($V_{SV} > V_{SH}$) sandwiched in between. The upper crustal anisotropy may reflect shallowly dipping layering within the Archean and adjacent imbricated nappe stacks, whereas the lower crustal anisotropy likely represents fossilized crustal flow during the postorogenic or synorogenic collapse of the Pan-African Orogen. The negative anisotropy layer may have preserved vertically oriented large shear zones of late Pan-African age. Within the Morondava basin, negative anisotropy in the uppermost ~5 km could have been generated by steep normal faults, jointing, and magmatic dike intrusions. The deeper sediments and underlying crustal basement are characterized by positive anisotropy. This is consistent with horizontal bedding in the sediments and with fabric alignment in the basement created by extension during the basin formation.

Key Points:
- Positive anisotropy in lower Precambrian crust attributed to crustal flow during PAO collapse
- Proterozoic shear zone system coincides with vertical fast direction of radial anisotropy
- Shallow negative anisotropy in Morondava basin shows imprint of vertical dike intrusions and faults

Supporting Information:
- Supporting Information S1
- Data Set S1

Correspondence to:
J. Dreiling,
dreiling@gfz-potsdam.de

Citation:
Dreiling, J., Tilmann, F., Yuan, X., Giese, J., Rindraharisaona, E. J., Rümpker, G., & Wysession, M. E. (2018). Crustal radial anisotropy and linkage to geodynamic processes: A study based on seismic ambient noise in southern Madagascar. *Journal of Geophysical Research: Solid Earth*, *123*, 5130–5146. https://doi.org/10.1029/2017JB015273

Received 21 DEC 2017
Accepted 30 MAY 2018
Accepted article online 5 JUN 2018
Published online 22 JUN 2018

1. Introduction

The island of Madagascar occupied a key region in both the assembly and breakup of Gondwana. Numerous geological investigations were carried out in and adjacent to Madagascar to understand the evolution of the former supercontinent (e.g., Bardintzeff et al., 2010; Coffin & Rabinowitz, 1988; Fritz et al., 2013; Geiger et al., 2004; Tucker et al., 2011, 2014). Little was known about the subsurface structure due to the lack of seismological data, except for studies of the structure below four of the permanent broadband stations (Rindraharisaona et al., 2013) and a model for the central region (Rambolamanana et al., 1997). Recently, several passive seismic deployments have been conducted in Madagascar, including SELASOMA (Tilmann et al., 2012), MACOMO (Wysession et al., 2011), and RHUM-RHUM (Barruol et al., 2017), which allow imaging of the seismic signatures of past geodynamic events in the crust and lithosphere of southern Madagascar. Here we use data recorded by these experiments to characterize the radial anisotropy in the crust of southern Madagascar based on Rayleigh and Love wave dispersion measured from ambient noise correlations.

1.1. Geodynamic Background

The geology of southern Madagascar is characterized by the crystalline basement, which covers the eastern two thirds of the island and comprises Archean and Proterozoic units, and by the sedimentary Morondava basin in the west (Figure 1). Both the crystalline basement and the Morondava basin are in some places intruded by Cretaceous volcanics, with significant outcrops along the east coast, in the area around Volcan de l'Androy in the south, and in the central Morondava basin (Roig et al., 2012). The formation of each unit

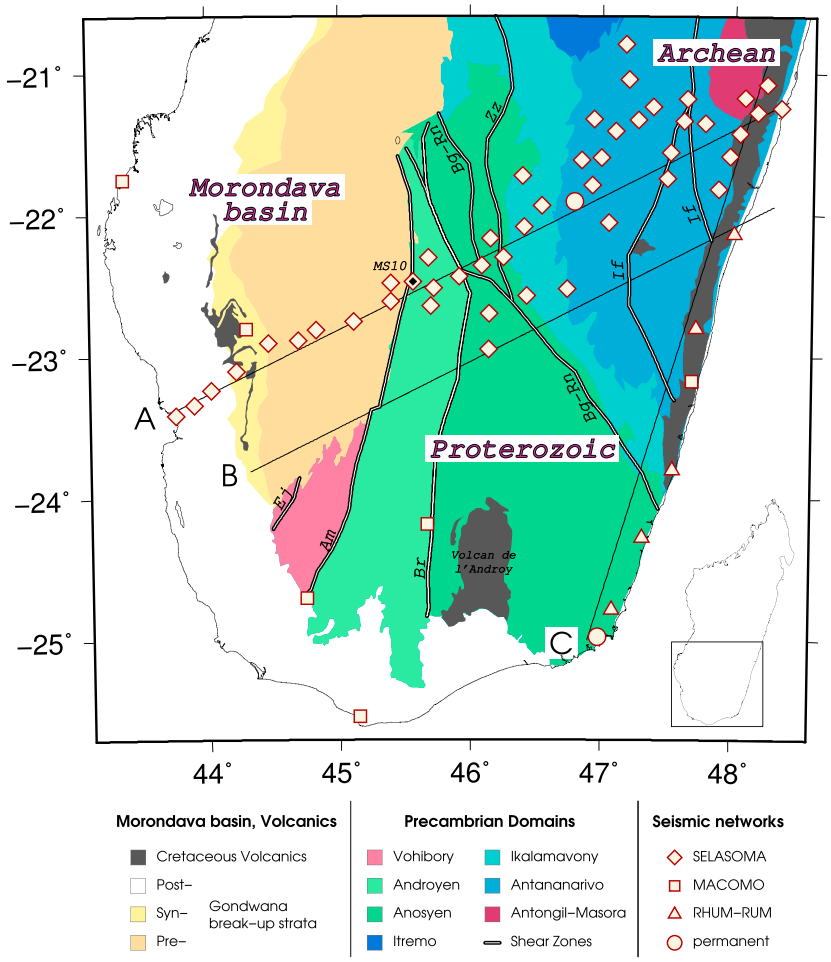

Figure 1. Simplified surface geology of southern Madagascar after Boger et al. (2008a, 2008b, 2008c), Roberts et al. (2012), and Tucker et al. (2011). Illustrated shear zones after Martelat et al. (2000): Ampanihy (Am), Bongolava-Ranotsara (Bg-Rn), Beraketa (Br), Ejeda (Ej), Ifanadiana (If), and Zazafotsy (Zz). Note that the shear zones represented here as lines often represent broader zones of deformation. Lines A–C signify locations of cross sections shown in Figure 6. Map data after Rindraharisaona et al. (2017).

is associated with a major episode in the geologic history of Madagascar: the crystalline basement represents the assembly of Gondwana finalized by the Pan-African Orogeny, the Morondava basin reflects the separation of Africa and Madagascar and also earlier failed rifting episodes, and Cretaceous volcanism accompanies the separation of Madagascar from India and the Seychelles.

The formation of proto-Madagascar was accomplished through the accretionary convergence of the Proterozoic southern domains (Vohibory, Androyen, Anosyen, and Ikalamavony) and the Archean units (Antananarivo and Antongil/Masora; Tucker et al., 2014). The stepwise accretion involved the subduction of back-arc basins and intervening oceans (Collins, 2006). The Ikalamavony domain has been interpreted as the volcano-sedimentary sequence of a magmatic arc accreted to the Antananarivo-Masora domains prior the Pan-African Orogeny in earliest Neoproterozoic time, subsequently followed by the formation of a passive continental margin with the deposition of associated sediments (i.e., Itremo; Boger et al., 2014). Renewed eastward subduction of the Mozambique Ocean in Cryogenian time (720–635 Ma) triggered magmatism (e.g., Tucker et al., 2014) and sedimentation of the future Anosyen domain sediments within an active fore-arc environment (Boger et al., 2014). Following the model of Boger et al. (2015), the intraoceanic island arc of the Vohibory domain collided with the microcontinent of the Androyen domain between 650 and 610 Ma, forming the Ampanihy shear zone and preceding the final collision and formation of the Beraketa shear zone between the eastern amalgamated domains (Masora/Antananarivo/Ikalamavony/Anosyen) and the western amalgamated fragment (Androyen/Vohibory).

During the Pan-African Orogeny all the basement units were finally assembled (e.g., Tucker et al., 2014). The Pan-African Orogen was finalized in the compressional stress regime during the final Gondwana-forming collision between roughly 590 and 530 Ma, accompanied with syntectonic to posttectonic granitic magmatism of the Ambalavao suite (e.g., Tucker et al., 2014). The finite strain pattern dominating the Precambrian of southern Madagascar is defined by large areas comprising shallowly dipping to subhorizontal foliations with E-W trending stretching lineations. These are bordered by an extensive, anastamosing shear zone network that was active during late stage Pan-African transpressional tectonics (Lardeaux et al., 1999; Martelat et al., 2000). Most of the shear zones visible today are located within the Proterozoic domains and are characterized by kilometer-wide zones of steeply dipping, highly strained rocks. While the Ampanihy and Beraketa shear zones represent terrane boundaries, the Ejeda, Bongolava-Ranotsara, Ifanadiana, and Zazafotsy shear zones run intradomainly (GAF-BGR, 2008). All these shear zones feature tight to isoclinal folds and are highly flattened crustal-scale zones resulting from the Pan-African collision. The Ranotsara zone shows ductile sinistral deflection confined to its central segment and prominent NW-SE trending brittle faulting along most of its length (Schreurs et al., 2010). The shear zones appear to be rooted in a zone of broadly distributed deformation in the crust or mantle (Reiss et al., 2016).

The collisional event caused crustal shortening and thickening (60–70 km), with subsequent thinning by a combination of lower crustal delamination (Rindraharisaona et al., 2017), gravitational spreading (de Wit et al., 2001; Fitzsimons, 2016; Giese et al., 2017), and upper crustal removal through erosion and exhumation (Giese et al., 2011; Seward et al., 2004). The central part of the East African Orogen reached thermal equilibrium between 500 and 350 Ma (Emmel et al., 2008), and Early Permian (ca. 290 Ma) limestones, deposited during the oldest marine transgression within central Gondwana (Wescott & Diggens, 1997), show that parts of the orogen were by then eroded to sea level (Emmel et al., 2008).

Compressive intraplate stress related to far-field stresses (effective mechanical coupling of orogenic belt and continental foreland) caused reactivation of basement faults, triggered the opening of intracontinental pull-apart basins through strike-slip displacement close to the Vohibory domain, and initiated the separation of Africa and Madagascar (Schandelmeier et al., 2004). The Ampanihy shear zone in particular appears to have influenced the opening of the southern Morondava basin. The kinematic character forming the Morondava basin gradually changed from transtensional sag dynamics to purely tensional tectonics (normal faulting) by the Early Triassic (Schandelmeier et al., 2004). The Phanerozoic sedimentary basin was formed in two rifting episodes in the Permo-Triassic and Jurassic, respectively (Geiger et al., 2004, and references therein). The continental failed rift (namely, Karoo rift) resulted in a thinned crust and moderate sedimentation. The second rifting stage is characterized by the East Africa/ Madagascar rift locus migration toward the west (Geiger et al., 2004), the continuous rifting, and the breakup from Africa along a strike-slip boundary with passive margin formation. Coexisting NW directed, low-angle normal faults effectively thinned the crust below the western Madagascar island (Andriampenomanana et al., 2017). The breakup was accompanied by the deposition of thick sedimentary sequences with a maximum thickness of up to 10 km (Pratt et al., 2017; Rindraharisaona et al., 2017). The strata exposed in the Morondava basin are classified, from east to west, as pre-, syn-, and post-Gondwana breakup sequences (Geiger et al., 2004).

Late Cretaceous volcanism (ca. 90 Ma) along Madagascar's east coast relates to the separation of Madagascar from India-Seychelles and thus the final phase of the stepwise breakup of Gondwana. Extensional rifting developed a volcanic margin and might have caused a thinner crust along the east coast through crustal extension (Rindraharisaona et al., 2017). Basaltic and rhyolitic magmas intruded the crust and formed dikes not only where volcanic outcrops are found, that is, along the eastern margin, the Volcan de l'Androy in the Anosyen domain, and within the pre- and syn-Gondwana breakup strata of the Morondava basin (Figure 1), but also within the basement of the Vohibory, Androyen, Anosyen, Ikalamavony, and Antananarivo domains (GAF-BGR, 2008; Martelat et al., 2014; Roig et al., 2012; Storey et al., 1995). Isotopic analyses suggest that a deep magma source plays an important role in the formation of the flood basalts (Storey et al., 1995, 1997). Neogene and Quaternary tectonic reactivation resulted in renewed volcanic activity and uplift (Roberts et al., 2012; Storey et al., 1995).

1.2. Radial Seismic Anisotropy

Radial seismic anisotropy describes seismic anisotropy with a vertical symmetry axis, which causes a difference in the wave speed of the vertically or horizontally polarized shear waves irrespective of their azimuth of propagation. We estimate vertically and horizontally polarized shear wave velocities (V_{SV} and V_{SH})

from Rayleigh and Love wave dispersion, respectively, and compute radial anisotropy (RA) and the anisotropic parameter ξ as defined by Anderson (1961).

$$\mathrm{RA} = (\xi - 1) \times 100\% \tag{1}$$

$$\xi = \left(\frac{V_{SH}}{V_{SV}}\right)^2 \tag{2}$$

In an isotropic medium, V_{SV} and V_{SH} are equal. A negative radial anisotropy indicates a faster seismic velocity of vertically rather than horizontally polarized shear waves ($V_{SV} > V_{SH}$), while a positive radial anisotropy implies a faster velocity of the horizontally polarized wave ($V_{SV} < V_{SH}$).

Velocity anisotropy can be produced by the intrinsic properties of the single minerals of crustal and mantle rocks, if these align along their crystallographic axes, which is known as crystallographic preferred orientation (CPO). The alignment results from finite strain in the dislocation creep regime (e.g., Karato & Wu, 1993). Because alignment is not perfect and the anisotropic properties of the different constituent minerals sometimes interact destructively, the anisotropy of the bulk rock is usually much less than that of its minerals. Effective anisotropy can also result from isotropic constituents, if heterogeneities on a scale much smaller than the wavelength show preferred orientations; such anisotropy from shape-preferred orientation (SPO) can arise from aligned microcracks, layering, or the organization of melt in dikes or sills. In many cases, the development of SPO is governed by the current or paleostress field (Wang et al., 2013).

Radial anisotropy in the shallow crust (<5–10 km) is primarily associated with the presence of oriented microfractures and cracks (Luo et al., 2013; Tatham et al., 2008; Weiss et al., 1999). Midcrustal anisotropy is often attributed to the CPO of micas, that is, biotite and muscovite (e.g., Nishizawa & Yoshino, 2001). Although micas crystallize into the monoclinic crystal system, they show a hexagonal type of anisotropy on crustal scales. An important contributor to anisotropy in the lower crust is amphibole (Kitamura, 2006; Tatham et al., 2008). Amphiboles have monoclinic and orthorhombic crystal systems but, as with micas and most of the deep crustal minerals, are quasi-hexagonal (Weiss et al., 1999).

Many geodynamic settings are correlated with either compressional or extensional tectonics: both regimes can cause alignment, reorientation, recrystallization, and growth of minerals oriented perpendicular—or at defined angles—to the stress direction. Many studies of radial anisotropy relate compressional regimes to vertical and extensional regimes to horizontal alignment of crustal minerals (e.g., Luo et al., 2013). However, both regimes can produce very variable orientations of minerals and anisotropy signatures (e.g., Mainprice & Nicolas, 1989). In each case, vertical and horizontal preferred orientations need to be seen in relation to the geodynamic background at the specific location. While a negative anomaly suggests anisotropic features that are steeply dipping to subvertical (60–90°), a positive radial anisotropy implies that the anisotropic features are subhorizontal to shallowly dipping (0–30°; Xie et al., 2013). The strength of radial anisotropy (RA in equation (1) is a measure of the consistency of material alignment (CPO), the degree of organization, and the contrast in material properties (SPO).

2. Data and Methods

2.1. Seismic Data and Processing

Continuous seismic data from 61 three-component stations from three temporary seismic networks and two permanent stations were used in the analysis (Figure 1). The SELASOMA passive seismic experiment (Tilmann et al., 2012), deployed during 2012-2014, provides the majority of our data. Twenty-five broadband stations formed a WSW-ENE oriented, 530-km-long profile from Toliary to Mananjary across southern Madagascar with interstation distances of 15–20 km. Another 23 short-period stations located around the eastern part of the profile supplemented the main profile for 1 year. Five stations deployed within the RHUM-RUM project (Barruol et al., 2017) covered the SE coast of Madagascar, together with permanent station FOMA (GEOSCOPE, 1982). Finally, we used a subset of stations from the MACOMO project (i.e., those south of 21°S; Wysession et al., 2011, and the permanent station VOI; GEOFON Data Centre, 1993).

The continuous data were recorded using different types of sensors (e.g., Guralp 3ESP, Trillium 240, Mark L4C-3D) and various sampling rates (i.e., 20, 50, and 100 Hz). For the ambient noise correlation method, it was necessary to first correct for these different recording conditions. The raw data were baseline-corrected by removing the linear trend, downsampled to 5 Hz with prior application of a low-pass filter to prevent

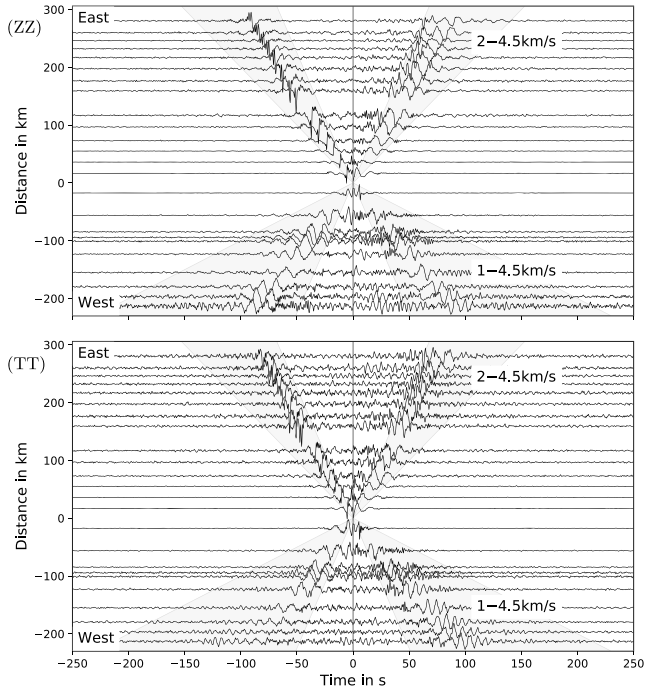

Figure 2. Record section of ZZ and TT correlograms with station MS10 at zero distance. Positive and negative distances are relative to MS10 and represent the interstation distances of stations located to the east and west, respectively. (MS10, as marked in Figure 1, is located at the boundary between the sedimentary basin to the west and the Precambrian units to the east). Correlograms have been filtered with a 1- to 35-s band pass. ZZ = vertical-vertical; TT = transverse-transverse.

aliasing effects, and the instrument response was removed. For ambient noise cross correlation we applied preprocessing procedures recommended by Bensen et al. (2007). The mean of all time series was subtracted then the data were clipped at 3 standard deviations and band-pass filtered between 0.01 and 1.25 Hz. Subsequently, spectral whitening and 1-bit normalization were applied. The cross correlation was performed by correlating 1-hr segments of all station and component combinations and subsequent rotation of the full Green's tensor stream from the ENZ to the RTZ coordinate system. The (maximum of) 24 correlograms resulting from 1 day were stacked and saved then cut to a length of 1,200 s (causal and acausal parts). Empirical Green's functions were estimated by stacking the daily stacks for the complete deployment period shared by both stations, that is, up to 747 days (median: 353 days). In total, we obtained multicomponent correlogram stacks for 1,847 station pairs. We assumed that the Rayleigh wave dispersion can be determined from the vertical-vertical (ZZ) correlograms and the Love wave dispersion from the transverse-transverse (TT) correlograms. For an approximately laterally homogeneous structure, this assumption is correct for Rayleigh waves, but the TT correlograms are in fact also weakly dependent on Rayleigh wave propagation (Haney et al., 2012). However, the small bias introduced by this is smaller than other sources of error within the period range of our measurements, so we neglect this minor effect here.

Figure 2 shows ZZ and TT correlograms sorted by station distance relative to station MS10, which is located at the boundary between the Phanerozoic sedimentary basin in the west and the Precambrian terranes in the east. Waves traveling through the sediments show a much longer wave train compared to the waves propagating through the hard rock, which is due to increased dispersion. While higher-frequency waves sample the surface and travel with the slower sedimentary velocities (later arrival times), the lower-frequency waves sample the deeper, faster crust. The Precambrian units of southern Madagascar contain little to no sediments; thus, waves propagate with nearly constant high velocities throughout the crust.

2.2. Dispersion Measurements and 2-D Tomography

To minimize possible errors due to automatic picking routines, we used a manual picking procedure for obtaining the fundamental mode group and phase velocity dispersion curves. Several properties of group velocities make it useful and preferable to include phase velocity observations (Boschi et al., 2012), which make the inversion results more robust. Particularly, at short periods it was not always possible to reliably pick the phase curves, so we opted to include both phase and group velocities in the inversion.

Group velocities were obtained by application of multiple-filter analysis following Dziewonski et al. (1969). The center frequencies of the narrow-bandwidth Gaussian filters range from 0.5 to 50 s with 150 discrete filter periods log spaced within this interval. Both the causal and acausal parts were taken into account for computing a stable envelope, whose peak at each period defined the dispersion curve. Instead of adding the traces for negative and positive time lags directly (as in Bensen et al., 2007), their envelopes were added after filtering. This procedure ensures constructive summation of the causal and acausal contributions. After Bensen et al. (2007), we considered only periods where a minimum of three wavelengths propagated within the interstation distance Δ. As the wave propagation velocity can be as high as 4 km/s, we conservatively assumed this velocity for the computation of the maximum reliable period T_{max} for each station pair, resulting in the condition $T < T_{max} = \Delta/12$.

Phase velocities were measured with the tool GSpecDisp (Sadeghisorkhani et al., 2017), which is based on the methodology of Ekström et al. (2009). It uses zero crossings of the real part of the correlation spectrum and interprets these in terms of phase velocity. The computation leads to a multitude of possible dispersion relations due to 2π ambiguity. For guiding the selection of the correct branch, we used the average dispersion curve for the study region as reference, which was computed based on the spatial autocorrelation of all correlograms (see Prieto et al., 2009).

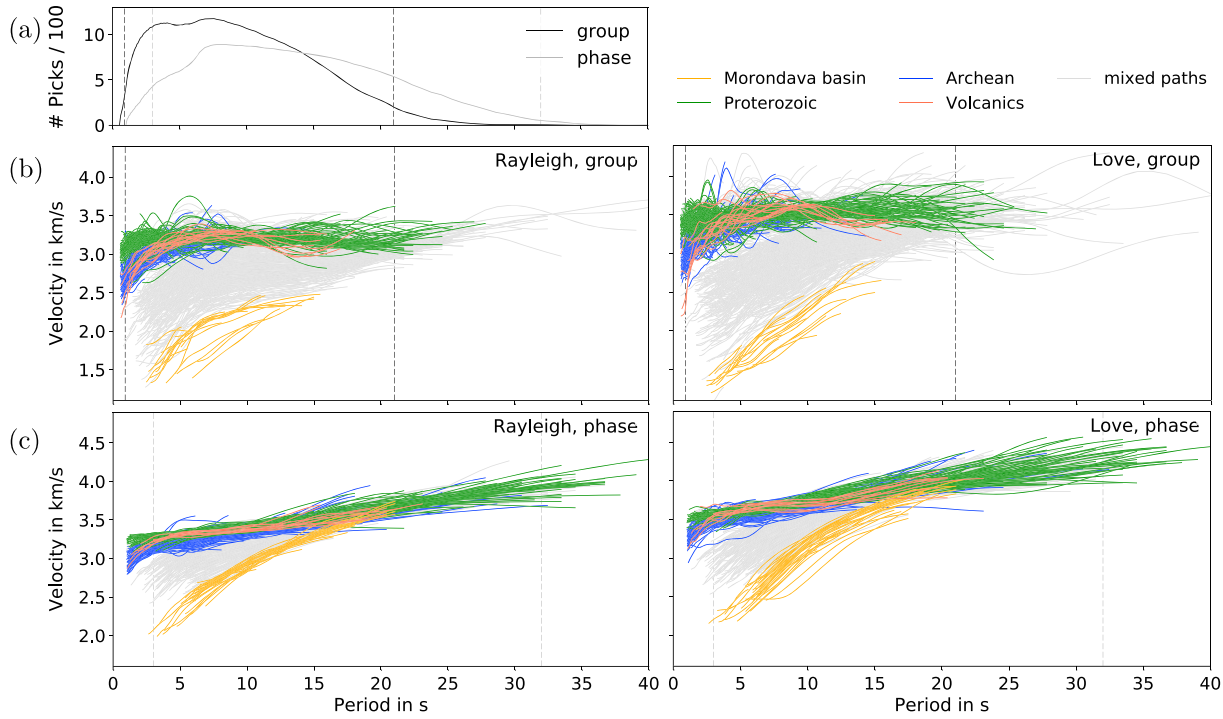

Figure 3. (a) Number of group and phase velocity picks used in the inversion; they are equal for Rayleigh and Love waves as common raypaths are used. Vertical lines represent the period intervals for the tomography. Region-dependent dispersion curves for Rayleigh and Love waves for (b) group and (c) phase velocities. Dispersion curves for paths fully contained within the Morondava basin, the Proterozoic or Archean blocks, or the coastal Cretaceous volcanics (for boundaries see Figure 1) are highlighted in color. Mixed dispersion relations plotted in gray represent raypaths encompassing more than one region.

During the picking process, each of the 2 × 1,847 surface wave time series was evaluated visually. If a period group velocity dependence was obvious and clear, the dispersion curve was picked. On the contrary, if the noise was too strong and the picking was unclear for the whole trace or for specific period ranges, then the station pair was discarded or the period range was not considered. Furthermore, the dispersion curve had to be smooth and continuous. The same criteria were used for phase velocity picking. Additionally, we estimated relative errors for group velocities from the width of the envelope peak for each period (more details in supporting information Figure S1) and used these as weighting factors in the 2-D inversions. The errors increase with period from 0.4 to 5.3 s (periods: 0.9–21 s) and are marginal larger for Love waves (~0.1 s). Within this period interval the corresponding velocity errors are 0.03–0.18 km/s. The dominant effect on the errors is the period (i.e., the narrow band-pass filter), which means that they are only comparable within a period. The method of error estimation was also used by, for example, Cotte and Laske (2002) and Harmon et al. (2007), and the errors represent the sharpness of the arrival time peaks in a relative sense rather than the conventional *measurement error* estimated by seasonal variations. Phase velocity errors were not estimated.

In total, 1,706 (1,495) group and 1,346 (1,087) phase velocity measurements were made for Rayleigh (Love) waves. Figure 3 displays an overview of all measured dispersion curves, showing the number of dispersion relations (a) and region-dependent trends, as well as a comparison of group and phase velocities (b, c). The dispersion curves for the different Precambrian units are quite similar, but the Morondava basin is clearly distinguished by low velocities at short periods. The phase velocity curves are smoother and less scattered than the group velocities, which primarily reflects the inherently lower precision of group velocity measurements (Boschi et al., 2012) and to a minor degree the larger sensitivity of group velocities to structural perturbations.

For the tomographic inversion, we only used station pairs for which both Rayleigh and Love wave dispersion could be measured. This reduced the number of measurements on average by 25% and 40% for Rayleigh (group and phase) and by 5% and 20% for Love waves (Figure 3a) but helped to increase the commensurability of the differently polarized wave types and thus reduced artifacts related to the different resolutions of Rayleigh and Love tomographic models.

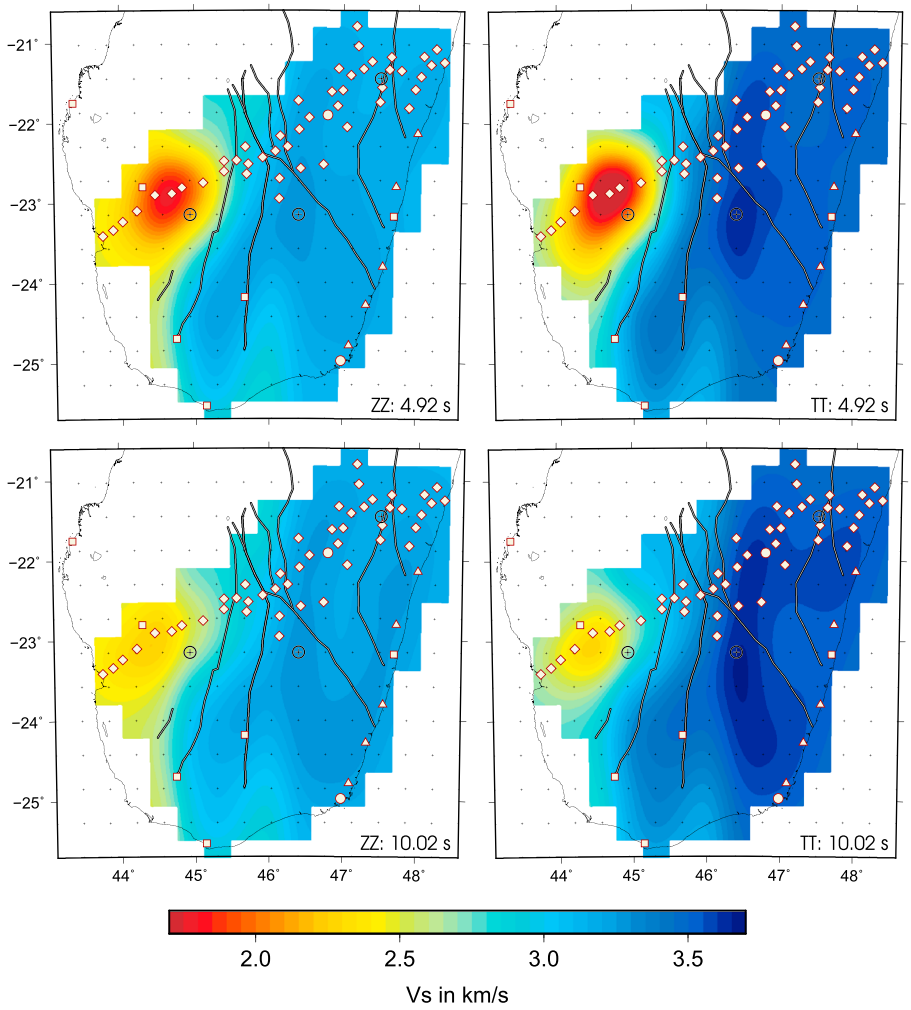

Figure 4. Tomographic results for Rayleigh (left column) and Love wave (right column) group velocities for 5- and 10-s period. For encircled grid nodes, inversion results are displayed in Figure 5.

The travel time tomography was performed using the Fast Marching Surface wave Tomography package (Rawlinson & Sambridge, 2005), which uses a finite-difference solution of the Eikonal equation to solve the forward problem and implements a subspace inversion to solve the inverse problem. This procedure is iterated several times, such that the raypaths adapt to the changing model, with outliers being removed at selected iterations.

The inversion grid covers exactly the area shown in Figure 1 and was gridded to 13×16 nodes with cell dimensions of about 47 and 37 km in latitude and longitude directions, respectively (Figure 4). A staircase model with two steps of increasing velocities toward the east was used as a starting model to reflect coarsely the large-scale structure. We initially tested starting models with a constant period-dependent velocity. However, the contrast between the sedimentary basins in the west and the Precambrian regions was so large that in the outlier removal stage many raypaths within the basin were erroneously declared as outliers.

Important parameters controlling the inversion include the damping factor, the smoothing factor (which constrains the smoothness of the inverted model), the number of iterations, and the percentage of outliers. Based on initial tests, we chose a smoothing factor of 3, a maximum number of 7 iterations, and an allowance of 1.5% outliers. Outliers are removed at iterations 3 and 5 and not recycled in ensuing iterations. In order to find the optimal damping factor for each period, we constructed trade-off curves from a set of 25 trial values (log spaced between 0.01 and 1,000). A selection of curves is illustrated in the supporting information (Figure S2). Our chosen damping factors represent a good compromise between minimizing the data misfit and model

variance. Because of the similarity of the optimum values for the Rayleigh and Love waves, we used their mean value for the final inversions of both group and phase velocities, respectively.

Group velocity results are illustrated in Figure 4 for two periods of each wave type. The RMS misfits are 2.3 and 1.9 s (ZZ) and 2.8 and 2.3 s (TT) for 5- and 10-s periods, respectively. These misfits cannot be directly compared to the error estimates as determined in the supporting information (average error there estimates 1.3 and 2.3 s for ZZ and 1.3 and 2.5 s for TT), because they are sensitive not only to the expected scatter but also to a period-dependent effect, which would be nonzero even for noise-free data. We note that the data-driven error estimates were used as weights in the inversion, but as each period is inverted separately, only their relative sizes at one period and for one wave type (Rayleigh or Love) matter.

The main feature revealed by the tomography (Figure 4) is the Morondava basin, with its low velocities in the west. The highest velocities are found in the central Precambrian units (Anoysen and Ikalamavony domains) along a N-S directed trend, which cuts across the Bongolava-Ranotsara zone. As expected, Love waves are on average 0.2–0.5 km/s faster than Rayleigh waves. In order to estimate the resolution of the tomographic models, we carried out a range of checkerboard tests (see supporting information Figure S3). Features as small as 2 × 2 grid cells (94 × 74 km) can be recovered at all periods along the main profile and along the east coast. Smearing occurs in the SW of the study region; its severity is period dependent and generally stronger for longer periods. Phase velocities are affected more severely. Features with dimensions larger than ~150–200 km are recovered fully throughout the region where ray coverage exists.

2.3. Velocity-Depth Inversion

The velocity-depth inversion was performed as a linearized least squares inversion as implemented in SURF96 from the toolbox *Computer Programs in Seismology* by Herrmann and Ammon (2002). From the 2-D tomography results, we constructed phase and group dispersion curves for a total of 96 grid nodes. The curves were boxcar smoothed around the central period (using a window width of seven period samples, corresponding to a width of ±10% of the center period) and cut to the period band selected for inversion (0.9–21 and 3–32 s). Phase and group dispersion curves were then jointly inverted. Although, in theory, the group dispersion curve can be derived from the phase curve, the measurement errors affecting both are different, such that the added redundancy provided by the group dispersion still helps to stabilize the inversion. Additionally, at short periods (0.9–3 s), only group velocity measurements are available. It was not possible to fit both Rayleigh and Love measurements with a single shear wave velocity model, which indicates the presence of radial anisotropy. We therefore inverted the Rayleigh and Love data separately and then computed the strength of radial anisotropy from their differences. Several studies apply a joint inversion and directly invert for anisotropy and average velocity. We are aware of this approach; however, the separate inversion approach is also justified both theoretically and from precedents in the literature (e.g., Chang et al., 2010; Guo et al., 2012).

We used the results of Rindraharisaona et al. (2017) to construct starting velocity models for the Rayleigh wave inversion. For the subsequent Love wave inversion, the final velocity structure derived from the Rayleigh wave inversion was used as the starting model (R→L ordered inversion). Thus, the Love wave inversion should introduce different velocities and thus radial anisotropy only when required by the data. To check whether these changes are robust and not random, the inversion was also performed the other way around: starting with the Love wave inversion, using starting models from the literature, followed by the Rayleigh wave inversion (L→R ordered inversion).

The 1-D model is parameterized with 0.5- and 1-km-thick layers within the uppermost 3 km, and 2.5-km steps down to 50.5 km, which are underlain by a half space. We chose a damping factor of 5, differential smoothing, and causal inversion coupling, and carried out 100 iterations. In order to test the dependence of the inversion on the starting model, we performed R→L and L→R ordered inversions using six different velocity models: two gradient models and four realistic models representing the subregions of southern Madagascar, that is, the Morondava basin, Proterozoic domains, Archean domains, and Cretaceous volcanics (along the east coast). The realistic models were generated from the results of Rindraharisaona et al. (2017) by taking the median velocity for each layer from the models for all stations in each subregion. Although each of the grid nodes is located in just one of the four subregions, we always tested all six starting models to assess the uniqueness of the inversion. We conclude that the effects of the starting model or the inversion order are not significant when it comes to radial anisotropy. A comparison of results is given in the supporting information (including Figures S5 and S6).

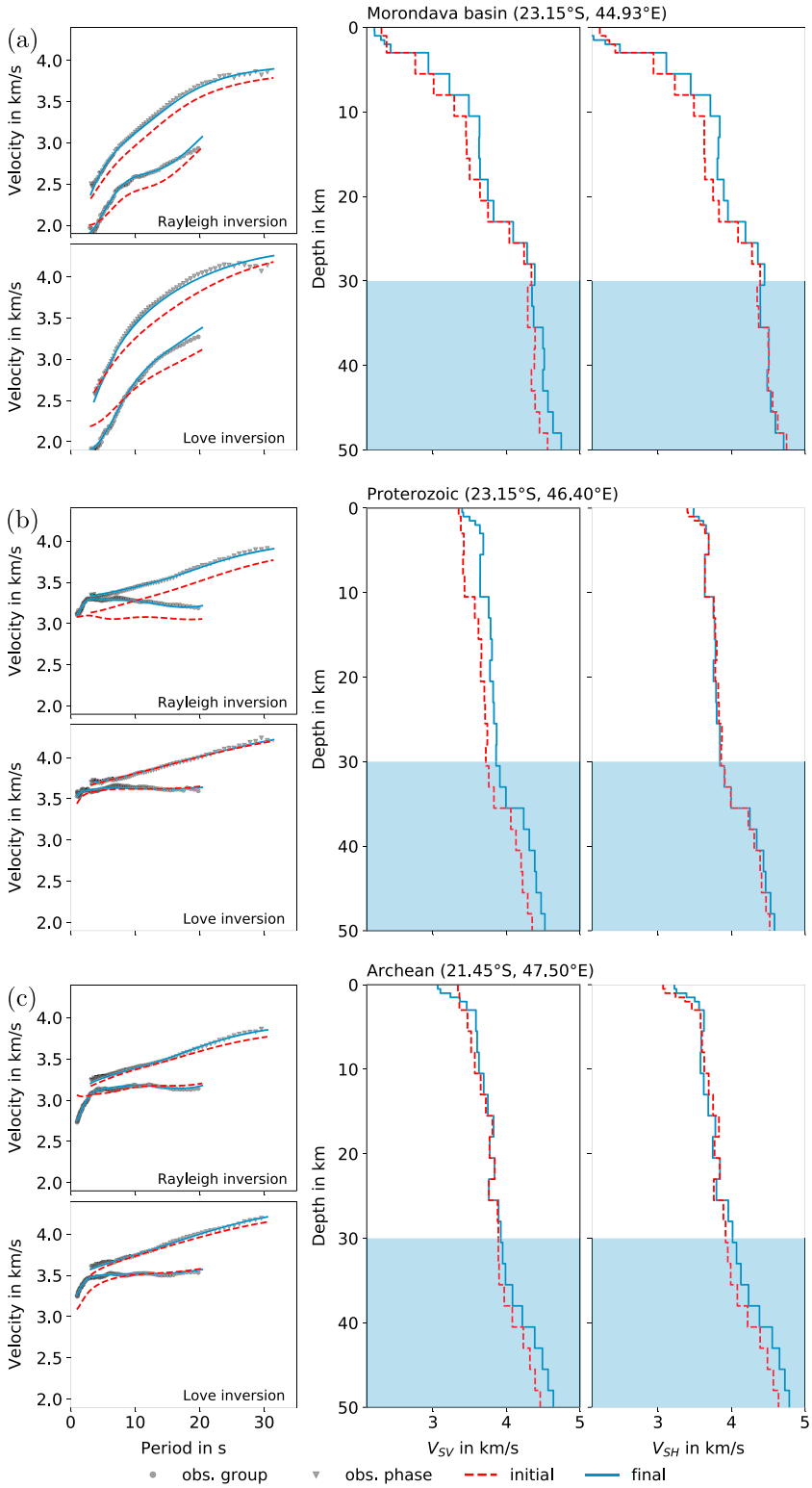

Figure 5. Joint velocity-depth inversion results for three grid nodes (a–c) located in different subregions as displayed in Figure 4. Each panel shows the data fit (first column) and starting and final velocity models for Rayleigh and Love wave inversions (second and third columns). The blue shaded areas represent depths where the data have little sensitivity and should not be interpreted.

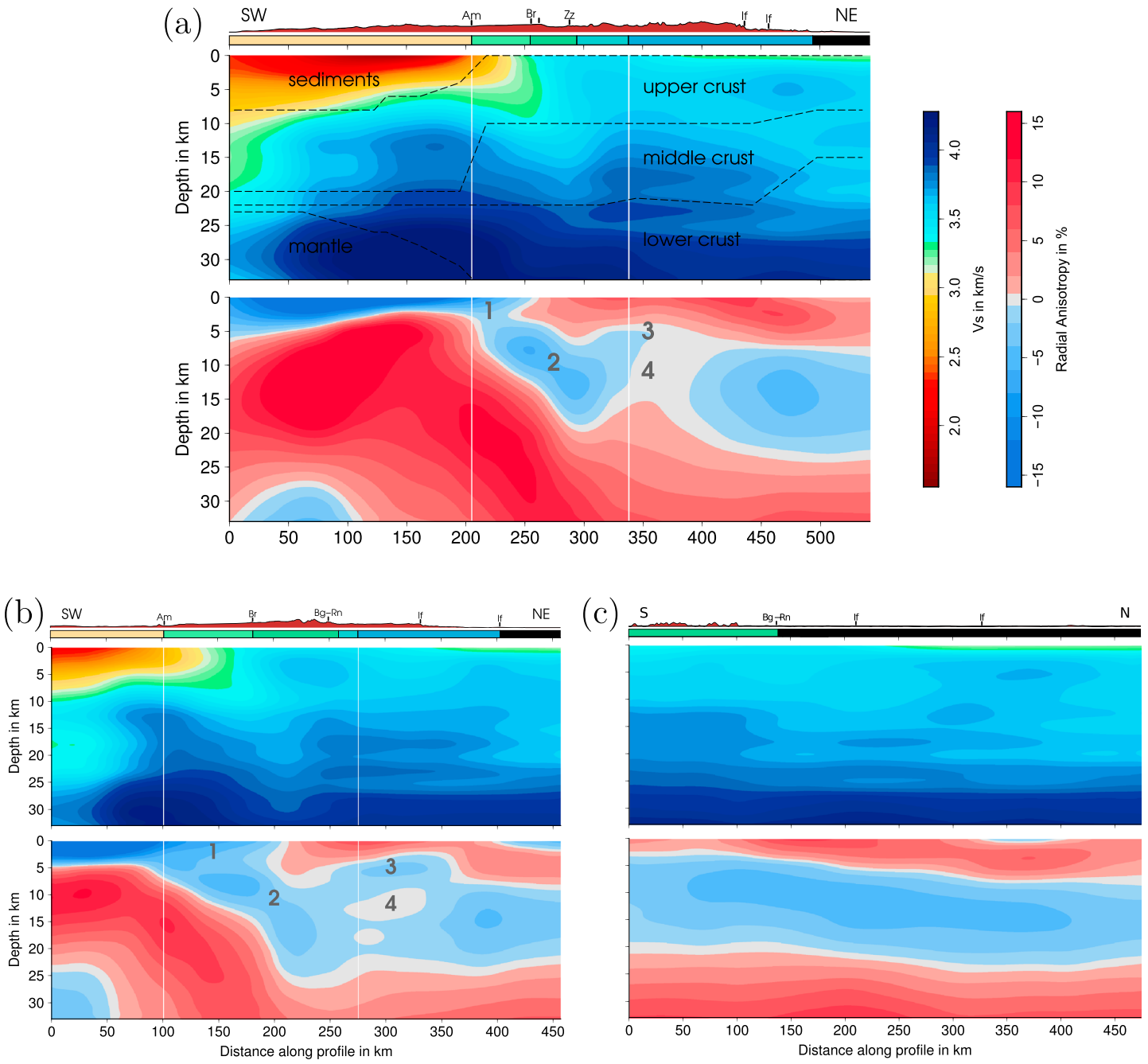

Figure 6. Cross sections showing mean V_S and radial anisotropy along profiles A–C (a-c) as indicated in Figure 1. Dashed lines (in a) mark the detailed crustal structure derived from the joint inversion of receiver functions and Rayleigh wave dispersions (Rindraharisaona et al., 2017). White lines indicate the vertical projection of surface contacts between Morondava basin and Proterozoic and Archean domains. Note that the actual orientation of contacts between these domains may not be vertical and may not extent through the entire depth range indicated. Features 1–4 are described in the text. The topography plot shows additional geologic divisions color coded as the units in Figure 1, except for the Morondava basin, which is unicolored. Elevation profile is based on etopo1 (Amante & Eakins, 2009).

Figure 5 shows multiple inversion results for three representative grid nodes in different subregions. The Rayleigh wave inversion requires larger velocity changes from the starting to the final model than the Love wave inversion because the starting model just represents a regional average. For the Love waves, the initial fit is already very good, so only small changes need to be introduced to accommodate the effect of radial anisotropy.

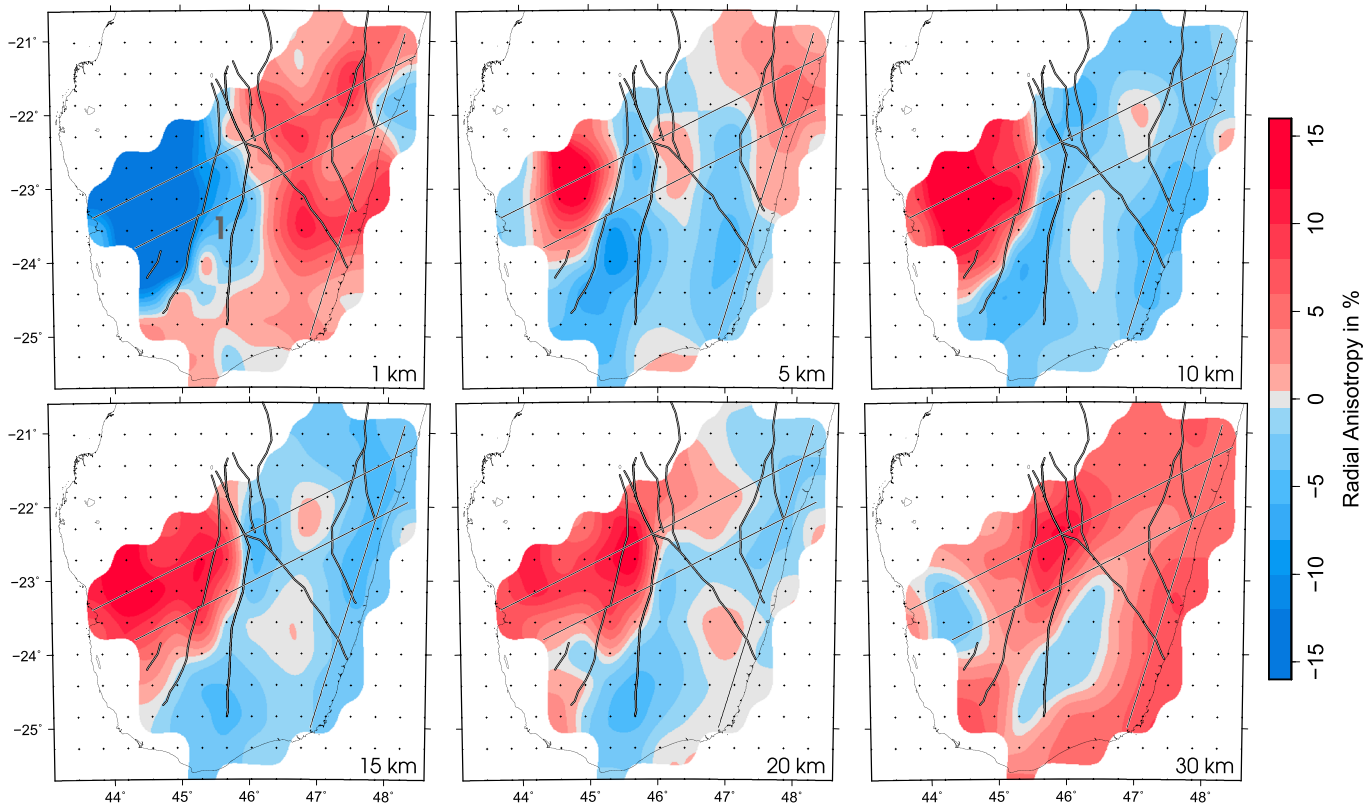

Figure 7. Radial anisotropy map view for depths of 1, 5, 10, 15, 20, and 30 km. See text for description of feature 1.

3. Shear Wave Velocity and Radial Anisotropy

In Figure 6, three representative cross sections of V_S and *RA* within our study area are shown, with locations as given in Figure 1. Additionally, horizontal slices at six different depths (1, 5, 10, 15, 20, and 30 km) can be seen in Figure 7. All results are from the R→L ordered inversion. For a comparison with the L→R ordered inversion, see the supporting information (Figure S6).

The velocity sections along the profiles (Figures 6a–6c, upper plots) show velocities increasing with depth. The low velocities (< 3.1 km/s) in the west of profiles A and B, extending to depths of 10 km, represent the Morondava basin. The middle crust is characterized by intermediate velocities along the east coast and high velocities beneath the Archean and the directly adjacent Proterozoic units. A strong lateral velocity change can be seen in the central Proterozoic unit, where the major shear zones are located. The corresponding radial anisotropy along profiles A and B (Figures 6a and 6b, lower plots) shows a complex pattern of positive and negative anomalies, which is almost the opposite when comparing the basin and the Precambrian region. Profile B shows a very similar anisotropic structure as Profile A, in particular, in association to the surface geology.

A pronounced negative radial anisotropy (> −12%) is revealed in the shallow part of the Morondava sediments with a thickness of 5 km beneath the western basin, thinning to 2 km below the eastern basin. The deeper basin and entire crust below it show a very high positive anisotropy, the strongest in our study region (> 12%). The mantle below the basin appears to show negative anisotropy, but it is close to the limit of our resolution. The Moho of Rindraharisaona et al. (2017) roughly follows the 5% anisotropy contour. The Precambrian units show a completely different depth dependency of RA: the uppermost upper crust (top, 5–8 km) is characterized by moderate positive values (mostly < 6%), down to 20-km depth, underlain by the middle crust with a moderately negative anisotropy (> −6%) and a lower crust with a positive anisotropy again. Beneath the Proterozoic units (Androyen and Anosyen), an easterly dipping negative anomaly (Figure 6, *feature 2*) seems to connect the shallow Morondava basin to the Precambrian middle crust, but because of the very different lithology, it is likely that the root causes are different. The anomaly dives from 5 km in the west down to a depth of 19 and 25 km in the east along profiles A and B, respectively (Figures 6a and 6b).

At the transition between the Proterozoic and Archean terranes (*feature 3*), the negative anomaly extends closer to the surface, reducing the thickness of the overlying positive anisotropy by 3 and 5 km in profiles A and B at 320–380 and 250–350 km, respectively. Within the negative RA layer in this part of the model (*feature 4*), the negative anisotropy is weaker (0–2%) in comparison to the adjacent units (2–6%). The anisotropy maps in Figure 7 emphasize the differences between the basin in the west and the Precambrian domains in the east. The second-order differences in the depth of the transition from positive to negative anomalies in the Precambrian domains are best appreciated in the 5-km depth section (Figure 7).

Profile C along the east coast (Figure 6c) shows a laterally nearly homogeneous layered anisotropy pattern: positive in the upper (< 8 km), negative in the middle (8–21 km), and positive in the lower crust (>21 km). This contribution is equivalent to the general Archean anisotropy pattern, although the middle-to-lower crustal contact is shifted to lie within the negative anisotropy using the boundaries defined by Rindraharisaona et al. (2017). The thickness of the shallow layer with positive anisotropy increases from 2 km in the south to 8 km in the north with the largest change approximately at the southern boundary of the volcanic units.

We consider all features discussed in the following as robust results of the inversion: Several tests have been performed to evaluate (1) the structural resolution of velocity anomalies (checkerboard tests), (2) the influence of the start velocities on the depth inversion (starting model tests), (3) the depth sensitivity of the data, (4) the possible creation of artifacts in the very shallow RA structure arising from the differences in the Love and Rayleigh sensitivity kernels at the same period, in particular with regard to the observed negative near-surface anisotropy in the sediments (sensitivity tests), and (5) the influence of the inversion order (R→L vs L→R). All these tests are mentioned in section 2 and are explained in detail in the supporting information.

4. Discussion

We obtained the radial anisotropic pattern for each of the major geological regions. The Proterozoic and Archean terranes reflect individual tectonic events of accretion and collision until they share a common history after amalgamation during the Pan-African collision (< 590 Ma). Along the east coast, additional volcanic prerift indicators, such as dikes and flood basalts from the Cretaceous, can be found (Storey et al., 1995). In contrast, western Madagascar underwent long-term rifting and sedimentary basin formation since roughly 300 Ma. Our interpretation of the current anisotropy pattern will consider inherited pre-Pan-African architecture, the Pan-African collision, which has modified most of the crust (Tucker et al., 2014), and the postorogenic tectonic evolution.

Proterozoic and Archean. Although featuring a rather complex tectonic history and diverse geology, the Precambrian domains (including the eastern coast) show a broadly similar anisotropy pattern, suggesting a strong influence of the late collisional and Gondwana forming event, the Pan-African Orogeny, on the generation of this background anisotropy. It is imaginable that the overall similar anisotropy indicates the postorogenic homogenization but also needs to be eyed carefully due to resolution limits of the applied method.

The Precambrian units are characterized by steeply or openly folded domains interrupted by kilometer-wide zones of steeply dipping, highly strained rocks and contact zones (Martelat et al., 2000; Tucker et al., 2011, and references therein). These shear zone structures are able to produce negative anisotropy if the fabric produced by shearing is subvertical. The Androyen and parts of the Anosyen domain show a negative surface anomaly (Figures 6 and 7, *feature 1*), which we assign to the strong isoclinal folding and vertical foliations within the shear zones (GAF-BGR, 2008). The midcrustal negative anisotropy within the Precambrian units could thus also reflect Pan-African vertical structures that were fossilized during subsequent lithospheric cooling (Walker et al., 2004) as manifested also by intradomain and interdomain shear zones across the southern island.

Preceding the final Pan-African collision, the Itremo and Ikalamavony domains were thrusted eastward onto the Antananarivo domain in central and southern Madagascar, respectively, forming an imbricated and relatively flat-lying nappe stack (e.g., Giese et al., 2017; Tucker et al., 2007). During the Pan-African Orogeny, this nappe stack and the Antananarivo domain in its footwall were intruded by large volumes of granitoid rocks of the Amabalavao suite (e.g., Tucker et al., 2014) resulting in large isotropic plutonic intrusions and also in form of foliation-parallel sills. Pan-African shortening affected this transitional part from the Proterozoic to the Archean domains (e.g., Giese et al., 2017), but its intensity decreases toward the east. This results in shallowly to moderately dipping foliation planes and open angle folds and preservation of inherited compositional

layering between orthogneisses and supracrustal formations within the Antananarivo domain (GAF-BGR, 2008), which could explain the faster *SH* velocities and thus a positive RA.

However, most of the Precambrian surface outcrops originated from middle-to-lower crust of the Pan-African Orogen and were buried to a depth of 25–35 km (Androyen domain; Jöns & Schenk, 2011) and 18–30 km (Anosyen domain; Horton et al., 2016, and references therein) presumably at the time of tectonic thickening of the crust (Horton et al., 2016). According to Horton et al. (2016), concentrated radiogenic heat production caused an extreme thermal anomaly in the middle crust (around 30 km) of southern Madagascar, which could have weakened it and initiated synorogenic or postorogenic crustal flow driven by the gravitational potential energy of the Pan-African Orogen. Evidence for late to postorogenic extension in this region of the Malagasy crust can be seen in low-angle extensional detachment faulting (Collins et al., 2000) and extensional reactivation of shallowly dipping ductile thrust contacts (Giese et al., 2017). Ductile flow is the main cause for textural alignment of minerals in metamorphic rocks (Rabbel et al., 1998) and is therefore also a plausible mechanism for the observed positive RA now observed in the shallowest layers in the eastern part of southern Madagascar, remembering that these rocks were in the middle crust at the beginning of the orogenic collapse.

Gravitational collapse is associated not only with midcrustal ductile flow but also with channeled lateral flow in the lower crust. Many studies point toward the latter, as this mechanism can accommodate collapse without surface extension being necessary (Rey et al., 2001, and references therein). The Tibetan plateau is the best modern analogue for the Pan-African collision zone (Fitzsimons, 2016; Horton et al., 2016). Radial anisotropy of the Tibet/ Himalaya region was examined in several studies (e.g., Chen et al., 2009; Duret et al., 2010; Guo et al., 2012; Huang, 2014; Shapiro et al., 2004). These studies typically observed a middle-to-lower crustal positive radial anisotropy. Duret et al. (2010) found a positive anomaly at 15- to 45-km depth, and Shapiro et al. (2004) found one at 25- to 50-km depth. Ambient noise studies discovered similar upper limits and even deeper lower limits for their study areas. Guo et al. (2012) found positive anisotropy in the midcrustal layer of southern Tibet (>25 km, limited by the maximum resolved depth of 35 km). Chen et al. (2009) analyzed the Qinghai-Tibet Plateau and surrounding regions and found almost exclusively positive anisotropy at a depth range of 18–75 km in the Himalayan, Lhasa, and Qiangtang blocks. Huang (2014) observed widespread positive anisotropy in zones (with low wave speeds) in the middle and lower crust (~20 km—Moho) of the southeastern Tibetan Plateau. The positive middle-to-lower crustal RA observations there are generally interpreted as crustal channel flow. It is likely that the positive anisotropy characterizing the Madagascar Precambrian basement at 20- to 30-km depth today was generated through similar mechanisms during the Pan-African collapse, when the layers were buried at depths of around 40–60 km. The anisotropic fabric formed in the Precambrian during the orogeny and subsequent collapse thus appears to have been preserved, even as the top layers of the crust were removed by erosion.

The RA structure of the Proterozoic and its interpretation differ in some important details from the adjacent Archean units. (1) The east dipping negative-positive anisotropy contrast within the Androyen and Anosyen domains (Figure 6, *feature 2 and below*) could be due to the composition of the crustal rocks causing a weaker rheology during final collision and indentation of the Antananarivo-Antongil-Masora block (Schreurs et al., 2010), resulting in much stronger deformation during shortening compared to the adjacent domains further east. With this in mind, the dipping anomaly (feature 2) could be the expression of the final Pan-African collision and suturing of the Mozambique Ocean, which was subducted eastward below the Anosyen-Ikalamavony-Antananarivo-Masora domains (Boger et al., 2015). The anomaly may thus simply trace the Androyen domain into the crust. (2) The extension of the Proterozoic negative anomaly to the surface (feature 1) might be the expression of the strongly upright folded and horizontally shortened large-scale vertical shear zones seen in the surface geology (GAF-BGR, 2008). Also, teleseismic shear wave splitting combined with forward modeling revealed an ~150-km-wide zone with a fast direction of azimuthal anisotropy −40° and up to 12% (azimuthal) anisotropy (Reiss et al., 2016). The later rifting, initiating and forming the Morondava basin in western Madagascar, could have overprinted midcrustal shear zone signatures below the negative anomaly within the Proterozoic domains by horizontal stretching; we note that the dipping negative RA anomaly occurs in the region of the largest gradient in Moho depth, increasing from about 28 to 38 km (profile A at 180–280 km in Figure 6a).

The Morondava basin. The positive radial anisotropy in the crust beneath the sediments is the expected consequence of long-lasting extension over a time of about 150 Ma. The basin formed as a result of horizontal stretching and thinning of the crust, likely permitting mineral alignment along the deformation direction.

Based on the absence of fast lower crustal velocities in the thinned crust below the basin, Rindraharisaona et al. (2017) argued that the crustal thinning might have been accomplished by exhumation of lower crust along a low-angle detachment; this motion would likewise be expected to result in subhorizontal mineral alignment. The western basin is the only place in our model where surface waves of the examined period range are sensitive to the structure of the mantle. Tests here show some dependence on the details of the inversion procedure (Figure S6), as this part of the model is close to the limit of resolution. Nevertheless, it is clear that negative RA is present in the mantle below the basin.

In the basin sediments themselves, the deeper positive RA is expected from SPO of alternating horizontal layers of different seismic velocities. The shallow negative RA is surprising, though, as there is no way to produce it from the SPO of isotropic layers. However, negative RA in the near surface in basin settings is not that unusual. Chen et al. (2009) found values of $-5 \pm 3\%$ down to depths of 8 km and deeper in the major Tarim and Qaidam basins adjacent to the Qinghai-Tibet Plateau. Shirzad and Shomali (2014) reported a negative anisotropy in the shallow (<2 km) Tehran basin of Iran, which they explained by the vertical alignment of cracks along the surface. Although the shallow Morondava basin contains jointing and is also spiked with rather steeply dipping normal faults (GAF-BGR, 2008), this might not be the exclusive explanation for the strong negative surface anisotropy, as the spacing between the faults is relatively wide and might not be able to generate an anisotropic effect stronger than the sedimentary layering itself. Instead, Cretaceous dike intrusions could generate strong lateral velocity contrasts within the sediments, which, with a minimum thickness and spacing, could overprint the RA signature of horizontal sedimentary layering. The presence of outcrops of cross-cutting Cretaceous dikes in the Cretaceous and parts of the adjacent Jurassic strata in the southern Morondava basin (Roig et al., 2012; Storey et al., 1995) supports this hypothesis for the western Morondava basin. Of course, the presence of surface outcrops of dikes implies that intrusions must be present throughout the sedimentary package, and this would influence the anisotropy. The positive RA in the deeper parts of the basin might also be enhanced by the intrusions, if they are organized predominantly as sills rather than dikes (Jaxybulatov et al., 2014).

No surface outcrops of volcanic rocks have been mapped in the eastern Morondava basin. However, it is conceivable that the Ejeda-Bekily dike swarm (between the Volcan de l'Androy and the Ejeda SZ) has intruded into the sediments, traversing the southernmost part of the Morondava basin without penetrating the recent surface but supporting the negative surface anisotropy. From a geological point of view, it seems rather unlikely that the young dike intrusions stop directly at the Ejeda shear zone (e.g., as illustrated in Roig et al., 2012). As the Cretaceous dikes are obviously located in the western part of the Morondava basin, we propose that a combination of magmatic intrusions, normal faults, and jointing is responsible for the negative surface anisotropy in the basin.

The Cretaceous volcanics. The radial anisotropy pattern along the east coast does not show a difference compared to the general Archean one. The large intrusions and flood basaltic extrusions do not seem to influence the signature of the radial anisotropy, although the velocities in the middle crust along the coast are smaller relative to the Archean ones (Figures 6a–6c). However, this region is at the edge of our study area and has a rather narrow width, so the surface waves with paths along the east coast would still be influenced by the Archean structure.

5. Conclusions

Fundamental differences in the anisotropic pattern are found between the amalgamated Precambrian units in the east and the Phanerozoic Morondava basin in the west. In the Precambrian terranes, positive anisotropy is found in the upper and lower crust, with a layer of negative radial anisotropy in between. In the western part of the Proterozoic terranes, the negative anomaly becomes shallower and meets the surface. Within the Morondava basin, negative anisotropy is observed in the uppermost sediments, whereas the lower sediments and the underlying crust are characterized by positive anisotropy.

Gravitational flow during the PA synorogenic or postorogenic collapse must have had an enormous role in the shaping of the lower and possibly also the shallow crustal structure of the Precambrian domains, causing differences in shear wave speeds between vertical and horizontal propagation directions. The positive RA of the uppermost layers may also reflect the overall shallowly dipping and gently folded compositional layering within the Archean domains and the imbricated nappe stack at the boundary to the Proterozoic domains.

However, since this portion of a highly overthickened crust was at depths affected by radiogenic heat production during the Pan-African collision (Horton et al., 2016; Jöns & Schenk, 2011), postorogenic collapse could have caused horizontal spreading also responsible for the anisotropic pattern. The lower crustal positive anomaly can thus be ascribed to fossil lower crustal flow (in analogy to the active flow inferred in Tibet; e.g., Huang, 2014, Shapiro et al., 2004).

The midcrustal zone of negative anisotropy within the Precambrian (PAO lower crust, top) represents a strong zone during the collapse, whose anisotropy was likely imprinted during the collision and preserved until today. We ascribe these negative values to the fossilization of vertically oriented anisotropy, caused by the strongly folded and sheared fabrics at depth (Martelat et al., 2000), and cropping out at the surface, that is, the Ampanihy and Beraketa shear zones (GAF-BGR, 2008; Tucker et al., 2011).

The positive radial anisotropy within the Morondava basin between ~5-km depth and the Moho corresponds to the extensional structures forming the sedimentary basin by crustal stretching and thinning. Horizontally layered sediments and Cretaceous sills possibly enhance the anisotropy. The negative surface anisotropy could be generated by a combination of steep normal faults, jointing, and magmatic dike intrusions, the latter especially in the westernmost basin, which has multiple outcrops of such intrusions.

Acknowledgments
We thank Guilhem Barruol (Université de La Réunion, France) for initiating, with others, the RHUM-RUM project, a French-German collaboration, and giving us access to the stations deployed by this project in Madagascar prior to their public release. The RHUM-RUM data are now open and can be accessed through the RESIF data center and other EIDA nodes. We acknowledge the Geophysical Instrument Pool Potsdam (GIPP) for supplying the instruments for the SELASOMA project and the GEOFON data center for hosting the project data. We are very grateful to all fieldwork participants from the Institute and Observatory of Geophysics Antananarivo, the GFZ, and the University of Frankfurt and also to the landowners in Madagascar hosting our stations. This research has been supported by the DFG, grants TI316/4-1, YU115/10-1, GI825/2-1, and RU886/11-1. Elisa Rindraharisaona acknowledges support by the Alexander-von-Humboldt society. Last but not least, we thank the reviewers, the Associate Editor, and Martha Savage for constructive comments and suggestions.

References

Amante, C., & Eakins, B. W. (2009). ETOPO1 1 arc-minute global relief model: Procedures, data sources and analysis, NOAA Technical Memorandum. NESDIS NGDC-24, National Geophysical Data Center NOAA.

Anderson, D. L. (1961). Elastic wave propagation in layered anisotropic media. *Journal of Geophysical Research*, *66*(9), 2953–2963. https://doi.org/10.1029/JZ066i009p02953

Andriampenomanana, F., Nyblade, A. A., Wysession, M. E., Durrheim, R. J., Tilmann, F., Julià, J., et al. (2017). The structure of the crust and uppermost mantle beneath Madagascar. *Geophysical Journal International*, *210*(3), 1525–1544. https://doi.org/10.1093/gji/ggx243

Bardintzeff, J.-M., Liégeois, J.-P., Bonin, B., Bellon, H., & Rasamimanana, G. (2010). Madagascar volcanic provinces linked to the Gondwana break-up: Geochemical and isotopic evidences for contrasting mantle sources. *Gondwana Research*, *18*, 295–314.

Barruol, G., Sigloch, K., & RHUM-RUM group (2017). RHUM-RUM experiment, 2011-2015, code YV (réunion hotspot and upper mantle—réunion's unterer mantel) funded by ANR, DFG, CNRS-INSU, IPEV, TAAF, instrumented by DEPAS, INSU-OBS, AWI and the Universities of Muenster, Bonn La Réunion. https://doi.org/10.15778/RESIF.YV2011

Bensen, G. D., Ritzwoller, M. H., Barmin, M. P., Levshin, A. L., Lin, F., Moschetti, M. P., et al. (2007). Processing seismic ambient noise data to obtain reliable broad-band surface wave dispersion measurements. *Geophysical Journal International*, *169*(3), 1239–1260. https://doi.org/10.1111/j.1365-246X.2007.03374.x

Boger, S. D., Ferreira, C., Hirdes, W., Schulte, B., Jenett, T., & Dallwig, R. (2008a). Carte geologique de Madagascar 1: 500 000, feuilles No 7 - Morondava.

Boger, S. D., Ferreira, C., Hirdes, W., Schulte, B., Jenett, T., & Dallwig, R. (2008b). Carte geologique de Madagascar 1: 500 000, feuilles No 11 - Ampanihy 12-Tôlanaro.

Boger, S. D., Ferreira, C., Hirdes, W., Schulte, B., Jenett, T., & Dallwig, R. (2008c). Carte geologique de Madagascar 1: 500 000, feuilles No 10 - Fianarantsoa.

Boger, S. D., Hirdes, W., Ferreira, C. A. M., Jenett, T., Dallwig, R., & Fanning, C. M. (2015). The 580–520ma Gondwana suture of Madagascar and its continuation into Antarctica and Africa. *Gondwana Research*, *28*(3), 1048–1060. https://doi.org/10.1016/j.gr.2014.08.017

Boger, S. D., Hirdes, W., Ferreira, C. A. M., Schulte, B., Jenett, T., & Fanning, C. M. (2014). From passive margin to volcano-sedimentary forearc: The Tonian to Cryogenian evolution of the Anosyen Domain of southeastern Madagascar. *Precambrian Research*, *247*, 159–186. https://doi.org/10.1016/j.precamres.2014.04.004

Boschi, L., Weemstra, C., Verbeke, J., Ekström, G., Zunino, A., & Giardini, D. (2012). On measuring surface wave phase velocity from station-station cross-correlation of ambient signal. *Geophysical Journal International*, *192*, 346–358.

Chang, S.-J., Van Der Lee, S., Matzel, E., & Bedle, H. (2010). Radial anisotropy along the Tethyan margin. *Geophysical Journal International*, *182*(2), 1013–1024. https://doi.org/10.1111/j.1365-246X.2010.04662.x

Chen, Y., Badal, J., & Zhang, Z. (2009). Radial anisotropy in the crust and upper mantle beneath the Qinghai-Tibet Plateau and surrounding regions. *Journal of Asian Earth Sciences*, *36*(4–5), 289–302. https://doi.org/10.1016/j.jseaes.2009.06.011

Coffin, M. F., & Rabinowitz, P. D. (1988). *Evolution of the conjugate East African-Madagascan margins and the Western Somali Basin Special Paper* (p. 78, Geological Society of America Special Paper 226). Boulder CO, USA: Geological Society of America.

Collins, A. S. (2006). Madagascar and the amalgamation of Central Gondwana. *Gondwana Research*, *9*(1–2), 3–16. https://doi.org/10.1016/j.gr.2005.10.001

Collins, A., Razakamanana, T., & Windley, B. (2000). Neoproterozoic extensional detachment in central Madagascar: Implications for the collapse of the East African Orogen. *Geological Magazine*, *137*(1), 39–51.

Cotte, N., & Laske, G. (2002). Testing group velocity maps for Eurasia. *Geophysical Journal International*, *150*(3), 639–650.

de Wit, M. J., Bowring, S. A., Ashwal, L. D., Randrianasolo, L. G., Morel, V. P. I., & Rambeloson, R. A. (2001). Age and tectonic evolution of Neoproterozoic ductile shear zones in southwestern Madagascar, with implications for Gondwana studies. *Tectonics*, *20*(1), 1–45. https://doi.org/10.1029/2000TC900026

Duret, F., Shapiro, N. M., Cao, Z., Levin, V., Molnar, P., & Roecker, S. (2010). Surface wave dispersion across Tibet: Direct evidence for radial anisotropy in the crust. *Geophysical Research Letters*, *37*, L16306. https://doi.org/10.1029/2010GL043811

Dziewonski, A., Bloch, S., & Landisman, M. (1969). A technique for the analysis of transient seismic signals. *Bulletin of the Seismological Society of America*, *59*, 427–444.

Ekström, G., Abers, G. A., & Webb, S. C. (2009). Determination of surface-wave phase velocities across USArray from noise and Aki's spectral formulation. *Geophysical Research Letters*, *36*, L18301. https://doi.org/10.1029/2009GL039131

Emmel, B., Jöns, N., Kröner, A., Jacobs, J., Wartho, J., Schenk, V., et al. (2008). From closure of the Mozambique Ocean to Gondwana breakup: New evidence from geochronological data of the Vohibory Terrane, Southwest Madagascar. *The Journal of Geology*, *116*(1), 21–38. https://doi.org/10.1086/524121

Fitzsimons, I. C. W. (2016). Pan-African granulites of Madagascar and southern India: Gondwana assembly and parallels with modern Tibet. *Journal of Mineralogical and Petrological Sciences*, *111*(2), 73–88. https://doi.org/10.2465/jmps.151117

Fritz, H., Abdelsalam, M., Ali, K., Bingen, B., Collins, A., Fowler, A., et al. (2013). Orogen styles in the East African Orogen: A review of the Neoproterozoic to Cambrian tectonic evolution. *Journal of African Earth Sciences*, *86*, 65–106. https://doi.org/10.1016/j.jafrearsci.2013.06.004

GAF-BGR (2008). Carte structurale de Madagascar 1:500 000.

GEOFON Data Centre (1993). GEOFON seismic network. https://doi.org/10.14470/TR560404

Geiger, M., Clark, D. N., & Mette, W. (2004). Reappraisal of the timing of the breakup of Gondwana based on sedimentological and seismic evidence from the Morondava Basin, Madagascar. *Journal of African Earth Sciences*, *38*(4), 363–381. https://doi.org/10.1016/j.jafrearsci.2004.02.003

Giese, J., Berger, A., Schreurs, G., & Gnos, E. (2011). The timing of the tectono-metamorphic evolution at the Neoproterozoic-Phanerozoic boundary in central southern Madagascar. *Precambrian Research*, *185*(3–4), 131–148. https://doi.org/10.1016/j.precamres.2011.01.002

Giese, J., Schreurs, G., Berger, A., & Herwegh, M. (2017). Kinematics and significance of a poly-deformed crustal-scale shear zone in central to south-eastern Madagascar: The Itremo–Ikalamavony thrust. *International Journal of Earth Sciences*, *106*(6), 2091–2108. https://doi.org/10.1007/s00531-016-1415-z

Guo, Z., Gao, X., Wang, W., & Yao, Z. (2012). Upper- and mid-crustal radial anisotropy beneath the central Himalaya and southern Tibet from seismic ambient noise tomography. *Geophysical Journal International*, *189*(2), 1169–1182. https://doi.org/10.1111/j.1365-246X.2012.05425.x

Haney, M. M., Mikesell, T. D., van Wijk, K., & Nakahara, H. (2012). Extension of the spatial autocorrelation (SPAC) method to mixed-component correlations of surface waves Mixed-component correlations in SPAC. *Geophysical Journal International*, *191*(1), 189–206. https://doi.org/10.1111/j.1365-246X.2012.05597.x

Harmon, N., Forsyth, D., & Webb, S. (2007). Using ambient seismic noise to determine short-period phase velocities and shallow shear velocities in young oceanic lithosphere. *Bulletin of the Seismological Society of America*, *97*(6), 2009–2023. https://doi.org/10.1785/0120070050

Herrmann, R., & Ammon, C. (2002). Computer programs in seismology: Surface waves receiver functions and crustal structure.

Horton, F., Hacker, B., Kylander-Clark, A., Holder, R., & Jöns, N. (2016). Focused radiogenic heating of middle crust caused ultrahigh temperatures in southern Madagascar. *Tectonics*, *35*, 293–314. https://doi.org/10.1002/2015TC004040

Huang, H. (2014). Ambient noise tomography for wavespeed and anisotropy in the crust of southwestern China (PhD thesis), Massachusetts Institute of Technology.

GEOSCOPE (1982). French Global Network of broadband seismic stations. Paris, France: Institut de Physique du Globe de Paris. https://doi.org/10.18715/GEOSCOPE.G

Jaxybulatov, K., Shapiro, N. M., Koulakov, I., Mordret, A., Landes, M., & Sens-Schöfelder, C. (2014). A large magmatic sill complex beneath the Toba caldera. *Science*, *346*(6209), 617–619. https://doi.org/10.1126/science.1258582

Jöns, N., & Schenk, V. (2011). The ultrahigh temperature granulites of southern Madagascar in a polymetamorphic context: Implications for the amalgamation of the Gondwana supercontinent. *European Journal of Mineralogy*, *23*(2), 127–156. https://doi.org/10.1127/0935-1221/2011/0023-2087

Karato, S., & Wu, P. (1993). Rheology of the upper mantle: A synthesis. *Science*, *260*, 771–778.

Kitamura, K. (2006). Constraint of lattice-preferred orientation (LPO) on *Vp* anisotropy of amphibole-rich rocks. *Geophysical Journal International*, *165*(3), 1058–1065. https://doi.org/10.1111/j.1365-246X.2006.02961.x

Lardeaux, J.-M., Martelat, J.-E., Nicollet, C., Pili, E., Rakotondrazafy, R., & Cardon, H. (1999). Metamorphism and tectonics in southern Madagascar: An overview. *Gondwana Research*, *2*(3), 355–362.

Luo, Y., Xu, Y., & Yang, Y. (2013). Crustal radial anisotropy beneath the Dabie orogenic belt from ambient noise tomography. *Geophysical Journal International*, *195*(2), 1149–1164. https://doi.org/10.1093/gji/ggt281

Mainprice, D., & Nicolas, A. (1989). Development of shape and lattice preferred orientations: Application to the seismic anisotropy of the lower crust. *Journal of Structural Geology*, *11*(1–2), 175–189.

Martelat, J.-E., Lardeaux, J.-M., Nicollet, C., & Rakotondrazafy, R. (2000). Strain pattern and late Precambrian deformation history in southern Madagascar. *Precambrian Research*, *102*(1–2), 1–20. https://doi.org/10.1016/S0301-9268(99)00083-2

Martelat, J.-E., Randrianasolo, B., Schulmann, K., Lardeaux, J.-M., & Devidal, J.-L. (2014). Airborne magnetic data compared to petrology of crustal scale shear zones from southern Madagascar: A tool for deciphering magma and fluid transfer in orogenic crust. *Journal of African Earth Sciences*, *94*, 74–85. https://doi.org/10.1016/j.jafrearsci. 2013.07.003

Nishizawa, O., & Yoshino, T. (2001). Seismic velocity anisotropy in mica-rich rocks: An inclusion model. *Geophysical Journal International*, *145*(1), 19–32. https://doi.org/10.1111/j.1365-246X.2001.00331.x

Pratt, M. J., Wysession, M. E., Aleqabi, G., Wiens, D. A., Nyblade, A. A., Shore, P., et al. (2017). Shear velocity structure of the crust and upper mantle of Madagascar derived from surface wave tomography. *Earth and Planetary Science Letters*, *458*, 405–417. https://doi.org/10.1016/j.epsl.2016.10.041

Prieto, G. A., Lawrence, J. F., & Beroza, G. C. (2009). Anelastic Earth structure from the coherency of the ambient seismic field. *Journal of Geophysical Research*, *114*, B07303. https://doi.org/10.1029/2008JB006067

Rabbel, W., Siegesmund, S., Weiss, T., Pohl, M., & Bohlen, T. (1998). Shear wave anisotropy of laminated lower crust beneath Urach (SW Germany): A comparison with xenoliths and with exposed lower crustal sections. *Tectonophysics*, *298*(4), 337–356. https://doi.org/10.1016/S0040-1951(98)00174-7

Rambolamanana, G., Suhadolc, P., & Panza, G. F. (1997). Simultaneous inversion of hypocentral parameters and structure velocity of the central region of Madagascar as a premise for the mitigation of seismic hazard in Antananarivo. *Pure and Applied Geophysics*, *149*(4), 707–730.

Rawlinson, N., & Sambridge, M. (2005). The fast marching method: An effective tool for tomographic imaging and tracking multiple phases in complex layered media. *Exploration Geophysics*, *36*(4), 341–350. https://doi.org/10.1071/EG05341

Reiss, M. C., Rümpker, G., Tilmann, F., Yuan, X., Giese, J., & Rindraharisaona, E. J. (2016). Seismic anisotropy of the lithosphere and asthenosphere beneath southern Madagascar from teleseismic shear wave splitting analysis and waveform modeling. *Journal of Geophysical Research: Solid Earth*, *121*, 6627–6643. https://doi.org/10.1002/2016JB013020

Rey, P., Vanderhaeghe, O., & Teyssier, C. (2001). Gravitational collapse of the continental crust: Definition, regimes and modes. *Tectonophysics*, *342*(3), 435–449.

Rindraharisaona, E. J., Guidarelli, M., Aoudia, A., & Rambolamanana, G. (2013). Earth structure and instrumental seismicity of Madagascar: Implications on the seismotectonics. *Tectonophysics*, *594*, 165–181. https://doi.org/10.1016/j.tecto.2013.03.033

Rindraharisaona, E. J., Tilmann, F., Yuan, X., Rümpker, G., Giese, J., Rambolamanana, G., & Barruol, G. (2017). Crustal structure of southern Madagascar from receiver functions and ambient noise correlation: Implications for crustal evolution. *Journal of Geophysical Research: Solid Earth*, *122*, 1179–1197. https://doi.org/10.1002/2016JB013565

Roberts, G. G., Paul, J. D., White, N., & Winterbourne, J. (2012). Temporal and spatial evolution of dynamic support from river profiles: A framework for Madagascar. *Geochemistry, Geophysics, Geosystems*, *13*, Q04004. https://doi.org/10.1029/2012GC004040

Roig, J., Tucker, R. D., Peters, S., Delor, C., & Théveniaut, H. (2012). Carte Gèologique de la Rèpublique de Madagascar à1 /1 / 1 000 000.

Sadeghisorkhani, H., Gudmundsson, O., & Tryggvason, A. (2017). GSpecDisp: A matlab GUI package for phase-velocity dispersion measurements from ambient-noise correlations. *Computers & Geosciences*, *110*, 41–53. https://doi.org/10.1016/j.cageo.2017.09.006

Schandelmeier, H., Bremer, F., & Holl, H. G. (2004). Kinematic evolution of the Morondava rift basin of SW Madagascar—From wrench tectonics to normal extension. *Journal of African Earth Sciences*, *38*(4), 321–330. https://doi.org/10.1016/j.jafrearsci.2003.11.002

Schreurs, G., Giese, J., Berger, A., & Gnos, E. (2010). A new perspective on the significance of the Ranotsara shear zone in Madagascar. *International Journal of Earth Sciences*, *99*(8), 1827–1847. https://doi.org/10.1007/s00531-009-0490-9

Seward, D., Grujic, D., & Schreurs, G. (2004). An insight into the breakup of Gondwana: Identifying events through low-temperature thermochronology from the basement rocks of Madagascar. *Tectonics*, *23*, TC3007. https://doi.org/10.1029/2003TC001556

Shapiro, N. M., Ritzwoller, M. H., Molnar, P., & Levin, V. (2004). Thinning and flow of Tibetan crust constrained by seismic anisotropy. *Science*, *305*(5681), 233–236.

Shirzad, T., & Shomali, Z. H. (2014). Shallow crustal radial anisotropy beneath the Tehran basin of Iran from seismic ambient noise tomography. *Physics of the Earth and Planetary Interiors*, *231*, 16–29. https://doi.org/10.1016/j.pepi. 2014.04.001

Storey, M., Mahoney, J. J., & Saunders, A. D. (1997). Cretaceous basalts in Madagascar and the transition between plume and continental lithosphere mantle sources. In J. J. Mahoney & M. F. Coffin (Eds.), *Large igneous provinces: Continental, oceanic, and planetary flood volcanism*, Geophysical Monograph Series. Washington, DC: American Geophysical Union. https://doi.org/10.1029/GM100p0095

Storey, M., Mahoney, J. J., Saunders, A. D., Duncan, R. A., Kelley, S. P., & Coffin, M. F. (1995). Timing of hot spot-related volcanism and the breakup of Madagascar and India. *Science*, *267*(5199), 852–855. https://doi.org/10.1126/science.267.5199.852

Tatham, D. J., Lloyd, G. E., Butler, R. W. H., & Casey, M. (2008). Amphibole and lower crustal seismic properties. *Earth and Planetary Science Letters*, *267*(1), 118–128. https://doi.org/10.1016/j.epsl.2007.11.042

Tilmann, F., Yuan, X., Rümpker, G., & Rindraharisaona, E. (2012). SELASOMA Project, Madagascar 2012–2014. https://doi.org/10.14470/MR7567431421

Tucker, R., Kusky, T., Buchwaldt, R., & Handke, M. (2007). Neoproterozoic nappes and superposed folding of the Itremo Group, west-central Madagascar. *Gondwana Research*, *12*, 32–56.

Tucker, R., Roig, J., Macey, P., Delor, C., Amelin, Y., Armstrong, R., et al. (2011). A new geological framework for south-central Madagascar, and its relevance to the "out-of-Africa" hypothesis. *Precambrian Research*, *185*(3–4), 109–130. https://doi.org/10.1016/j.precamres. 2010.12.008

Tucker, R., Roig, J., Moine, B., Delor, C., & Peters, S. (2014). A geological synthesis of the Precambrian shield in Madagascar. *Journal of African Earth Sciences*, *94*, 9–30. https://doi.org/10.1016/j.jafrearsci.2014.02.001

Walker, K. T., Nyblade, A. A., Klemperer, S. L., Bokelmann, G. H. R., & Owens, T. J. (2004). On the relationship between extension and anisotropy: Constraints from shear wave splitting across the East African Plateau. *Journal of Geophysical Research*, *109*, B08302. https://doi.org/10.1029/2003JB002866

Wang, N., Montagner, J.-P., Fichtner, A., & Capdeville, Y. (2013). Intrinsic versus extrinsic seismic anisotropy: The radial anisotropy in reference Earth models. *Geophysical Research Letters*, *40*, 4284–4288. https://doi.org/10.1002/grl.50873

Weiss, T., Siegesmund, S., Rabbel, W., Bohlen, T., & Pohl, M. (1999). Seismic velocities and anisotropy of the lower continental crust: A review. *Pure and Applied Geophysics*, *156*(1–2), 97–122. https://doi.org/10.1007/s000240050291

Wescott, W. A., & Diggens, J. N. (1997). Depositional history and stratigraphical evolution of the Sakoa Group (Lower Karoo Supergroup) in the southern Morondava Basin, Madagascar. *Journal of African Earth Sciences*, *24*(4), 585–601. https://doi.org/10.1016/S0899-5362(97)00082-1

Wysession, M. E., Wiens, D. A., & Nyblade, A. A. (2011). Investigation of sources of intraplate volcanism using PASSCAL broadband instruments in MAdagascar, the COmores, and MOzambique (MACOMO), International Federation of Digital Seismograph Networks.

Xie, J., Ritzwoller, M. H., Shen, W., Yang, Y., Zheng, Y., & Zhou, L. (2013). Crustal radial anisotropy across eastern Tibet and the western Yangtze craton. *Journal of Geophysical Research: Solid Earth*, *118*, 4226–4252. https://doi.org/10.1002/jgrb.50296